

See discussions, stats, and author profiles for this publication at: <https://www.researchgate.net/publication/231232749>

# Synthesis of Nanostructured Tungsten Oxide (WO<sub>2.9</sub>) Fibers and Discs

ARTICLE *in* CRYSTAL GROWTH & DESIGN · NOVEMBER 2009

Impact Factor: 4.89 · DOI: 10.1021/cg900544k

---

CITATIONS

11

---

READS

172

5 AUTHORS, INCLUDING:



V. Shukla

Rutgers, The State University of New Jersey

27 PUBLICATIONS 217 CITATIONS

SEE PROFILE

Synthesis of Nanostructured Tungsten Oxide (WO<sub>2.9</sub>) Fibers and DiscsJ. F. Al-Sharab,<sup>\*,†</sup> R. K. Sadangi,<sup>†</sup> V. Shukla,<sup>†</sup> S. D. Tse,<sup>‡</sup> and B. H. Kear<sup>†</sup><sup>†</sup>Center for Nanomaterials Research, and <sup>‡</sup>Mechanical & Aerospace Engineering, Rutgers University  
Piscataway, New Jersey 08854

Received May 20, 2009; Revised Manuscript Received August 27, 2009

**ABSTRACT:** Evaporation of WO<sub>3.0</sub> powder during transmission electron microscopy resulted in the formation of nanofibers of WO<sub>2.9</sub>, which deposited on adjacent cooler regions of the carbon substrate. Controlled experiments using the inert gas condensation method were performed to investigate the formation mechanism of the nanofibers. Depending on the growth conditions, different morphologies of WO<sub>2.9</sub> phase were observed. Structural characterization was carried out using analytical electron microscopy techniques. On the basis of these observations, a qualitative growth model is proposed.

## Introduction

Tungsten trioxide (WO<sub>3-x</sub>) phases have been the subject of extensive research<sup>1–4</sup> because of their growing technological importance. The materials have applications in gas and humidity sensors,<sup>5</sup> electronic information displays, color memory devices, photoelectric sensors, superconductors, electrochromic devices, ferroelectrics,<sup>6–8</sup> Li-ion batteries,<sup>9,10</sup> and semiconductors.<sup>6</sup> This wide range of applications is due to the large number of crystalline forms displayed by WO<sub>3-x</sub> phases, which include cubic, orthorhombic, tetragonal, monoclinic, and several perovskite structures, depending on the processing environment and oxygen partial pressure.<sup>2,11,12</sup> Recently, various methods have been reported for preparing tungsten oxide nanowires and nanostructures.<sup>13–19</sup> However, methods capable of synthesizing high quality nanostructured WO<sub>3-x</sub> phases are still lacking.<sup>13</sup> Some progress has been made in preparing WO<sub>3</sub> nanorods by heating a tungsten tip<sup>14</sup> and by thermal oxidation.<sup>13</sup> However, these techniques still lack the ability to control orientation and defect density. Here, a new method is described for synthesizing WO<sub>2.9</sub> nanofibers and nanodiscs that display a high degree of crystalline perfection.

The new method was discovered during routine transmission electron microscopy (TEM) observations of orthorhombic WO<sub>3.0</sub> nanopowders. When the electron-beam intensity was increased sufficiently, a small portion of the nanopowder experienced vaporization, likely by sublimation, and the vaporized species then condensed to form nanofibers on adjacent cooler regions of the carbon substrate. Further analysis showed that the nanofibers were highly perfect single crystals of tetragonal WO<sub>2.9</sub>. The long axis or growth direction of the nanofibers was [110], and their flat surfaces were predominantly (001), that is, parallel to the basal plane of the tetragonal structure.

Follow-up inert gas condensation (IGC) experiments were carried out to simulate the TEM environment. The main components of the inert gas chamber and experimental set up are shown in Figure 1. In IGC, the powder is evaporated in a low-pressure vacuum chamber, and the vaporized species

are collected on a water-cooled chill plate. Nanofibers are formed at various locations on the chill plate, whereas elongated nanofibers are prevalent on sections of the chill plate nearest to the evaporative source.

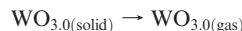
## Experimental Section

The starting WO<sub>3.0</sub> powder was synthesized by heating ammonium metatungstate, that is, (NH<sub>4</sub>)<sub>6</sub>H<sub>2</sub>W<sub>12</sub>O<sub>40</sub>·xH<sub>2</sub>O, to 500 °C in air. X-ray diffraction (XRD) analysis of the yellow powder confirmed that it had an orthorhombic crystal structure. The powder was evaporated in both TEM and IGC systems.

In the TEM case, a sample of WO<sub>3.0</sub> powder was first dispersed in trichloro-trifluoroethane. Then, a drop of the suspension was placed on a “lacy” carbon film supported on a copper grid, and dried. After insertion into the TEM, the electron beam was focused near the edge of a cluster of particles, and nanofibers were observed to form on the adjacent cooler carbon substrate.

In the IGC case, a sample of WO<sub>3.0</sub> powder was placed in a tungsten boat and evaporated in a reduced pressure (0.05 torr) of high purity argon. The evaporated species deposited on an Al foil attached to a water-cooled steel plate. The chill plate was oriented so that its thin edge was located above the tungsten heater, with a 5 mm stand-off distance. Samples were collected at various locations in the thermalizing zone just above the evaporative source, Figure 1. A similar experiment was conducted without any cooling water to examine the effect of substrate temperature. Temperature was measured at various locations on the collection plate with thermocouples attached to the surface of the plate, Figure 1. Temperature profiles for cooled and uncooled plates are plotted in Figure 2.

In order to investigate the decomposition of WO<sub>3.0</sub> into WO<sub>2.9</sub>, free energy calculations were performed using standard thermochemical data based on the solid → vapor → solid transformation. The reactions and changes in free energy are as follows:



$$\Delta G = \Delta H - T\Delta S = -561.10 - 0.18033T (\text{Joule})$$

The calculated logarithmic variations of partial pressures of WO<sub>3</sub> and O<sub>2</sub> in a closed vacuum system are plotted in Figure 3. Under vacuum conditions existing in TEM (~10<sup>-7</sup> torr) and IGC (~0.05 torr), vaporization of WO<sub>3</sub> should occur at ~675 °C in the TEM and at ~1150 °C in the IGC. IGC experiments were performed based on these calculations.

Scanning electron microscopy (SEM) observations were made using a field-emission SEM with energy dispersive spectroscopy

\*Corresponding author: Jafar F. Al-Sharab, Ph.D. Rutgers, The State University of New Jersey, Department of Materials Science and Engineering McLaren Center for Ceramic Research, 607 Taylor Road, Room 237, Piscataway, NJ 08854-8065. Tel.: 732-445-5615. Fax: 732-445-3258. E-mail: jafarhan@rci.rutgers.edu.

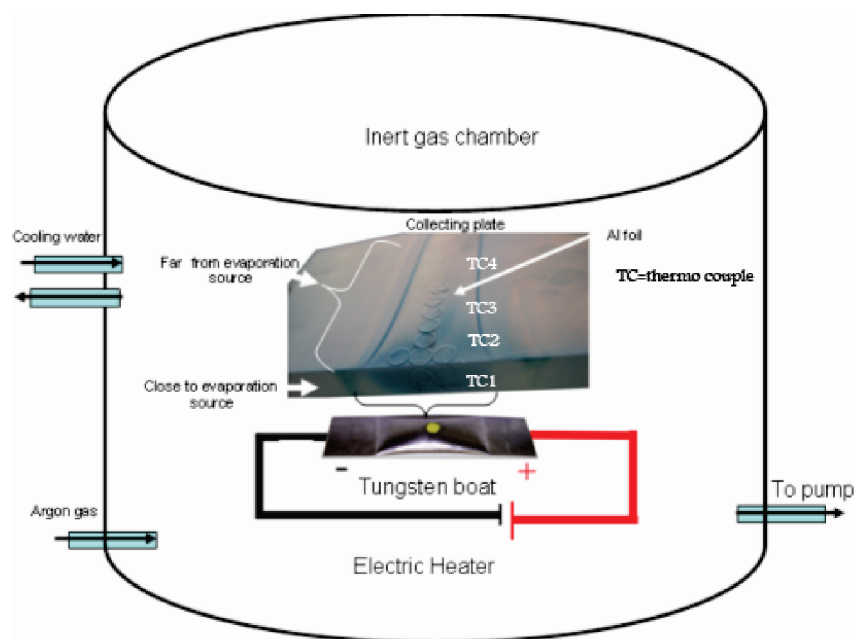


**Figure 1.** Schematic diagram of inert gas condensation (IGC) process showing the experimental setup and locations on the collecting plate where samples were collected.

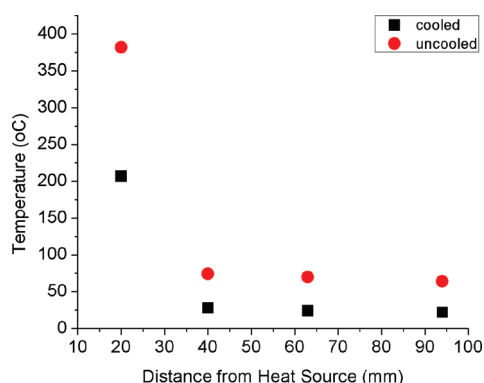


**Figure 2.** Temperature profile of collecting plate with and without water cooling.

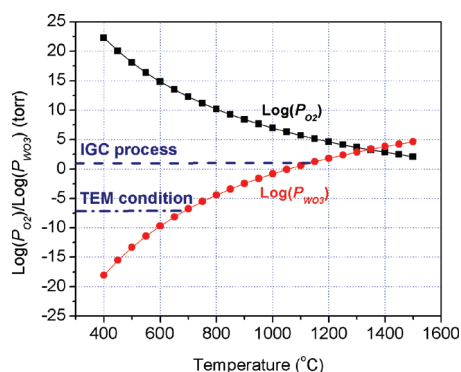


**Figure 3.** Vapor pressures of  $\text{WO}_{3.0}$  ( $P_{\text{WO}_{3.0}}$ ) and  $\text{O}_2$  ( $P_{\text{O}_2}$ ) as a function of temperature, as calculated from thermochemical data.

(EDS) attachment. Grain or crystallite size was determined by high resolution transmission electron microscopy (HRTEM). Intensity analyses of selected area electron diffraction (SAED) patterns were made using Process-Diffraction software.<sup>20</sup> Simulations of SAED

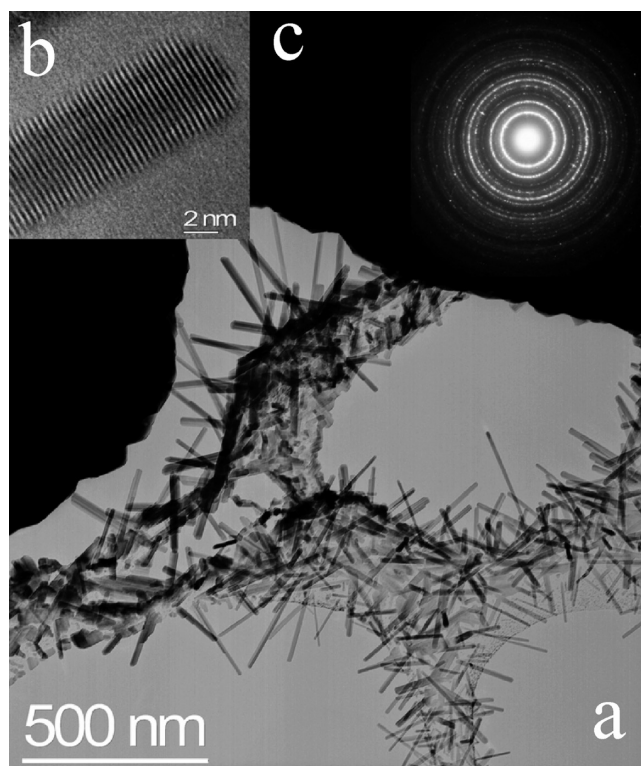


**Figure 4.** (a) Bright field TEM image of the  $\text{WO}_{2.9}$  nanofibers grown in situ in TEM; (b) high resolution TEM image of an individual nanofiber with 0.374 nm spacing of (110) planes; (c) SAED pattern of the nanofibers.

patterns were performed using Java electron microscopy (JEMS) software.<sup>21</sup>

## Results and Discussion

Various  $\text{WO}_{2.9}$  particle morphologies were observed after evaporation of  $\text{WO}_{3.0}$  powder in TEM and IGS systems.



**Table 1.** Indexing of Diffraction Patterns of TEM and IGC Grown Particles<sup>a</sup>

<i>d</i> -spacings from TEM grown nanofibers (Å)	<i>d</i> -spacings from IGC grown nanodiscs (Å)	standard tetragonal WO <sub>2.9</sub> ( <i>P4/nmm</i> (124))		standard monoclinic WO <sub>2.92</sub> ( <i>P2/c</i> (13))	
		<i>d</i> -spacings (Å)	( <i>h k l</i> )	<i>d</i> -spacings (Å)	( <i>h k l</i> )
				4.1700	( $\bar{1}$ 0 14)
				3.8200	(0 1 0)
3.757	3.746	3.7400	(1 1 0)		
				3.6800	( $\bar{1}$ 0 16)
3.127	3.107	3.1000	(1 0 1)		
				2.7100	( $\bar{4}$ 0 12)
2.661	2.650	2.6500	(2 0 0)	2.6500	( $\bar{1}$ 1 16)
2.205	2.171	2.2000	(2 0 1)	2.2100	( $\bar{4}$ 1 12)
	2.002	2.0200	(2 1 1)		
1.874	1.855	1.8800	(2 2 0)	1.8780	(6 0 6)
	1.768	1.7800	(1 0 2)	1.6952	( $\bar{1}$ 2 16)
1.679	1.655	1.6700	(3 1 0)	1.6853	(3 2 5)
1.545	1.543	1.5300	(3 1 1)		
		1.4800	(2 1 2)		
1.332	1.343	1.3300	(4 0 0)		
	1.300				
1.251	1.25	1.2500	(3 3 0)		
1.181	1.164	1.1700			

<sup>a</sup>The *d*-spacings of standard tetragonal WO<sub>2.9</sub> and monoclinic WO<sub>2.92</sub> along with their corresponding planes are presented for comparison.

Three distinct particle morphologies were identified: (i) nanodiscs, (ii) nanofibers, and (iii) nanorods.

**Nanofibers Formed in the TEM.** Figure 4a shows a bright field image of WO<sub>2.9</sub> fibers after exposure to a high intensity electron beam. Nanofibers are formed in bands on the carbon substrate adjacent to the electron-beam impingement zone. The fiber dimensions are inversely proportional to their distance from that zone. Typically, the fibers are ~400 nm in length and ~30 nm in diameter. A high resolution lattice image, Figure 4b, shows that the fibers are defect-free single crystals. In a few cases, small twins are observed in fibers with diameters > 25 nm.

Electron diffraction of an area containing many such nanofibers, Figure 4c, shows continuous concentric rings, indicating random orientation of very fine fibers. Analysis of the diffraction pattern is given in Table 1. In this table, *d*-spacings along with their corresponding planes are given and compared to two standard structures: tetragonal WO<sub>2.9</sub> (space group *P4/nmm*) and monoclinic WO<sub>2.92</sub> (space group *P2/c*). The data show that the nanofibers have WO<sub>2.9</sub> chemistry, tetragonal structure, and [110] growth direction. Tungsten and oxygen only are detected by EDS analysis. Nucleation and growth of nanofibers, therefore, must have occurred without the assistance of a catalyst. This conclusion is supported by the absence of visible catalyst particles at the tips of the fibers, Figure 4b.

It has been reported<sup>1</sup> that reductive decomposition of WO<sub>3,0</sub> occurs at temperatures > 625 °C. Moreover, as noted above, thermodynamic chemical calculations also indicate that reduction of WO<sub>3</sub> to WO<sub>2.9</sub> can occur in the low oxygen partial pressure environments of TEM (~10<sup>-7</sup> Torr) and IGC (~0.05 Torr) systems. When a high intensity electron beam impinges on WO<sub>3</sub> particles, the localized increase in temperature causes evaporation or sublimation. Subsequent condensation of the vaporized species in the low oxygen environment leads to the growth of WO<sub>2.9</sub> nanofibers,

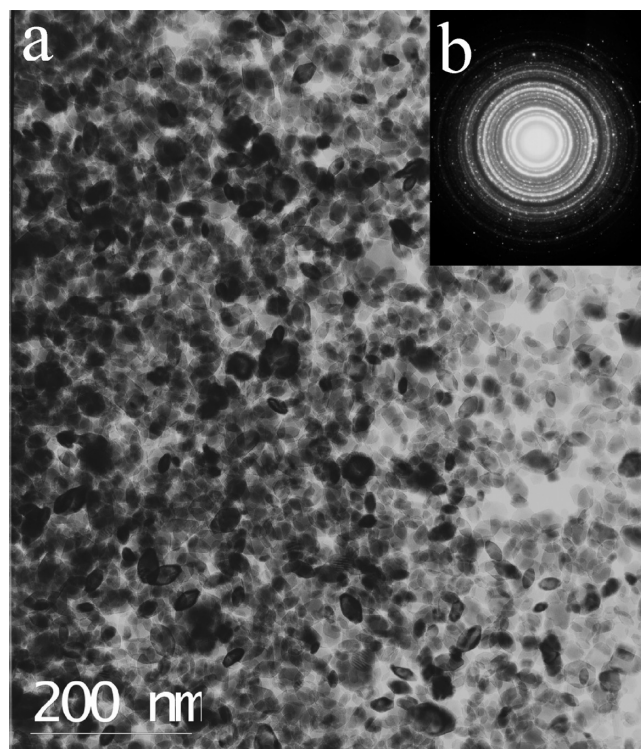


**Figure 5.** (a) Bright field image of disk-shaped WO<sub>2.9</sub> nanoparticles grown in the IGC system; (b) SAED pattern of nanodiscs.

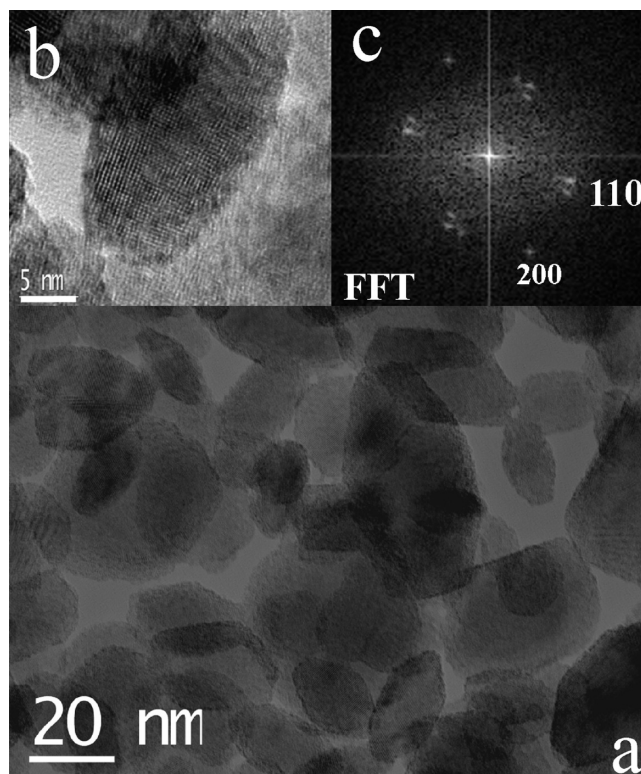


**Figure 6.** High-resolution TEM images of disk-shaped WO<sub>2.9</sub> nanoparticles.

apparently nucleating at ledges in the carbon film. Nanofibers grow in length by a tip-accretion mechanism and thicken by a ledge-growth mechanism.

**Nanostructures Formed in the IGC.** To evaluate the influence of substrate temperature on the morphology of con-

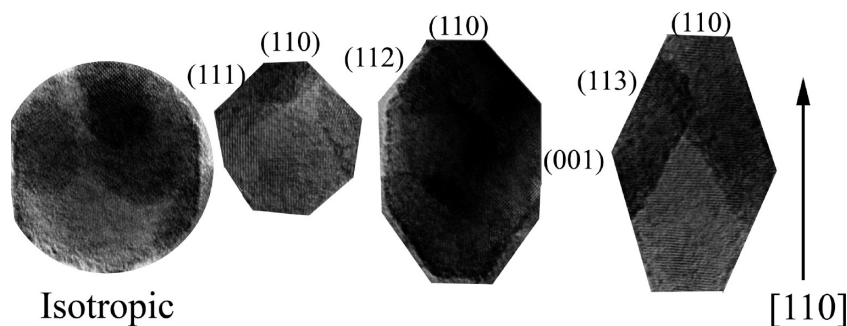


Figure 7.  $\text{WO}_{2.9}$  particles with different aspect ratios and faceting.

Table 2. Orientation Relationship and Estimates of Relative Surface Energy of Certain Planes in Tetragonal  $\text{WO}_{2.9}$

(hkl)	calculated angle between (110) and hkl (deg)	estimated relative surface energies of particles faceted along the 111	estimated relative surface energies of particles faceted along the 113	estimated relative surface energies of particles faceted along the 112
221	26.1	$\gamma_{110}/\gamma_{001} = 0.75$	$\gamma_{110}/\gamma_{113} = 0.5$	$\gamma_{110}/\gamma_{112} = 0.73$
111	44.4	$\gamma_{111}/\gamma_{001} = 0.57$		$\gamma_{110}/\gamma_{001} = 0.5$
112	62.9	$\gamma_{110}/\gamma_{111} = 1.38$		
113	71.2			
001	90			

densified  $\text{WO}_{2.9}$  nanoparticles, IGC processing was carried with and without water cooling of the substrate.

Nanostructures generated by vapor condensation on the water-cooled substrate are primarily in the form of faceted discs. Figure 5 shows a bright field image and diffraction pattern of disk-shaped nanoparticles. Indexing of the diffraction pattern gives a good match to the  $P4/nmm$  tetragonal  $\text{WO}_{2.9}$  phase, Table 1. Figure 6 shows a high resolution image of the same particles. The indexed spots in the fast Fourier transform (FFT) patterns correspond to the (110) and (200) planes with  $[00\bar{1}]$  zone axis. Hence, the major axis of a typical faceted particle is parallel to the  $[110]$  direction. The double spots in the FFT pattern are due to overlap of two crystals that share a common  $z$ -axis.

Close examination revealed disk-shaped nanoparticles with different aspect ratios and faceting, Figure 7. All faceted nanoparticles have a common base (110) with varying exposed planes. An increase in the aspect ratio results in the evolution of particle shape from spherical isotropic to polyhedron, Figure 7. These effects can be attributed to varying growth conditions at different locations from the vapor source. The faceting is due to minimization of surface energy, according to the Wulff theorem.<sup>22</sup> A summary of the relative surface energies estimated from the imaged particles are given in Table 2 using Wulff's theorem in reverse.<sup>23</sup> Currently, there are no available data in the literature on surface energies of  $\text{WO}_{2.9}$  crystals.

In addition to disk-shaped nanoparticles, nanorods were observed in regions of the chill plate closest to the evaporative source. Figure 8 shows a bundle of faceted nanorods, which are 30–200 nm in diameter and up to 7  $\mu\text{m}$  long. The rods have  $\langle 110 \rangle$  growth direction and thicken by a ledge-growth mechanism. The proximity of these rods to the evaporative source demonstrates that a high deposition rate may be needed for their formation. EDS analysis showed that the elements present are tungsten and oxygen only, so that a catalyst is not needed for rod growth.

A surprising finding was the formation of large aggregates (2–10  $\mu\text{m}$  diameter) of faceted nanoparticles (50–200 nm diameter) when the water cooling to the substrate was turned off, Figure 9a–d. Although most of the aggregates have a spherical morphology, a few displayed a remarkable

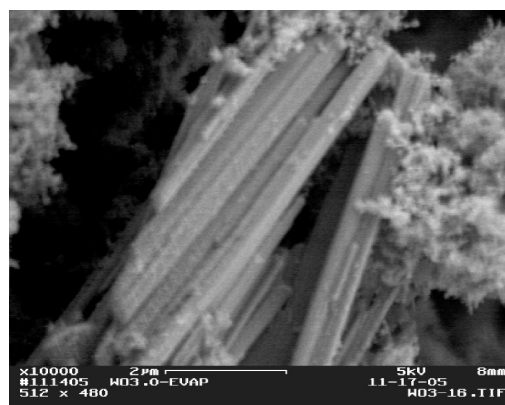


Figure 8. SEM images of the  $\text{WO}_{2.9}$  rods.

artichoke-like morphology. Nanoparticle aggregation may be ascribed to partial sintering when deposition and substrate temperatures are increased due to the absence of water cooling.

Results of our IGC and TEM experiments were compared to a recent study by Gallea et al.<sup>24</sup> on the effect of pressure and temperature on the formation of tungsten oxide nanostructures by thermal oxidation. On the basis of the pressure–temperature phase diagram from their experimental results, we might expect our IGC system, under the same temperature and pressure conditions, to grow  $\text{WO}_{2.9}$  thin films with a cooled substrate and  $\text{WO}_{2.9}$  rods with an uncooled substrate. On the contrary, our results are quite different, apparently due to the use of  $\text{WO}_{3.0}$  as starting material (versus W), and the introduction of Ar gas, allowing a different reaction route to occur. Irrespective of the different morphologies obtained, both results show a strong dependence of morphology on substrate temperature and oxygen partial pressure in the evaporation chamber.

The IGC process, therefore, has the ability to synthesize  $\text{WO}_{2.9}$  nanopowders with various morphologies, depending on substrate temperature and location from the evaporative source. Hence, it is potentially an attractive method for the production of such nanostructures.



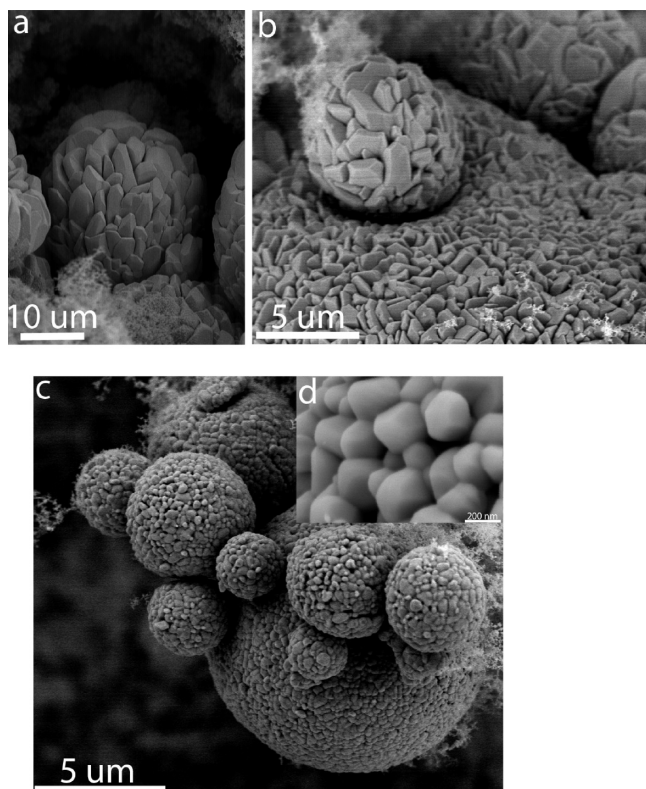


**Figure 9.** SEM images show various morphologies observed upon evaporation of  $\text{WO}_{3.0}$  onto an uncooled plate. Images (a) and (b) display an artichoke structure. Image (c) shows spherical growth morphology consisting of aggregated single crystal nanoparticles, (d).

### Conclusions

Nanostructures of  $\text{WO}_{2.9}$  are formed by electron-beam induced evaporation in the TEM. A similar behavior occurs when evaporation occurs in an IGC system. Depending on the growth conditions, different morphologies of  $\text{WO}_{2.9}$  are observed including nanofibers, nanodiscs, and nanorods. All the morphologies observed in these experiments have  $[110]$  growth direction. HRTEM imaging of the faceting of single crystal nanodiscs permitted an estimation of the relative surface energies.

**Acknowledgment.** This research was supported by ONR Grant N00014-01-1-0079 and ARO Grant W911NF-08-1-0417.

Special thanks are due to Ms. Cassandra D'Esposito and Mr. Jonathan Doyle for assistance with the experiments.

### References

- (1) Kear, B. H.; Wu, L.; Angastiniotis, N. C.; McCandlish, L. E. *Advanced Topics in Materials Science and Engineering*; Plenum Press: New York, 1993; pp 315–332.
- (2) Locherer, K. R.; Chrosch, J.; Salje, E. K. H. *Phase Transitions* **1998**, 67 (1), 51–58.
- (3) Locherer, K. R.; Swainson, I. P.; Salje, E. K. H. *J. Phys.: Condens. Matter* **1999**, 11, 4143–4156.
- (4) Gillet, M.; Delamare, R.; Gillet, E. *Eur. Phys. J.* **2005**, D 34, 291–294.
- (5) Chen, C.-H.; Wang, S.-J.; Ko, R.-M.; Kuo, Y.-C.; Uang, K.-M.; Chen, T.-M.; Liou, B.-W.; Tsa, H.-Y. *Nanotechnology* **2006**, 17, 217–223.
- (6) Alison, A.; Salje, E. K. *J. Phys.: Condens. Matter* **1998**, 10, L377–L380.
- (7) Salje, E. K. *Acta Crystallogr., Sect. B: Struct. Sci.*, **1977**, B33, 574–579.
- (8) Granqvist, C. G. *Solar Energy Materials & Solar Cells, Review of Progress 1993–1998* **2000**, 60, 201–262.
- (9) Poizot, P.; Laruelle, S.; Grugeon, S.; Dupont, L.; Tarascon, J. M. *Nature* **2000**, 407, 496–499.
- (10) Julien, C.; Haro-Poniatowski, E.; Camacho-Lopez, M. A.; Escobar-Alarcon, L.; Jimenez, J. J. *Mater. Sci. Eng. B* **1999**, 65, 170–175.
- (11) Howard, C. J.; Lica, V.; Knight, K. S. *J. Phys.: Condens. Matter* **2002**, 14, 377–387.
- (12) Al-Sharab, J. F.; Sadangi, R. K.; Shukla, V.; Kear, B. H. *Microsc. Microanal.* **2006**, 12, Suppl. 2, 1182CD–1183.
- (13) Liu, J.; Zhan, Y.; Zhang, Z. *J. Phys.: Condens. Matter* **2003**, 15, L453–L461.
- (14) Zhang, H.; Feng, M.; Liu, F.; Liu, L.; Chen, H.; Gao, H.; Li, J. *Chem. Phys. Lett.* **2004**, 389, 337–341.
- (15) Hong, K.; Yiu, W.; Wu, H.; Gao, J.; Xie, M. *Nanotechnology* **2005**, 16, 1608–1611.
- (16) Wang, S.-J.; Chen, C.-H.; Chang, S.-C.; Wong, C.-H.; Kai-Ming Uang, K.-M.; Chen, T.-M.; Ko, R.-M.; Liou, B.-W. *Nanotechnology* **2005**, 16, 273–277.
- (17) Li, Y.; Bando, Y.; Golberg, D. *Adv. Mater.* **2003**, 15, 1294–1296.
- (18) Zhou, J.; Ding, Y.; Deng, S. Z.; Gong, L.; Xu, S. N.; Wang, Z. L. *Adv. Mater.* **2005**, 17, 2107–2110.
- (19) Xu, F.; Tse, S. D.; Al-Sharab, J. F.; Kear, B. H. *Appl. Phys. Lett.* **2006**, 88, 243115-1-3.
- (20) Lábár, J. *Proceedings of EUREM 12, Brno*; Frank, L.; Ciampor, F., Eds.; Czechoslovak Society for Electron Microscopy, 1379, 2000.
- (21) Stadelmann, P., [http://cimewww.epfl.ch/people/stadelmann/jemsSE/jemsSEv3\\_2710u2008.htm](http://cimewww.epfl.ch/people/stadelmann/jemsSE/jemsSEv3_2710u2008.htm).
- (22) Wulff, G. Z. *Kristallogr. Mineral* **1901**, 34, 449.
- (23) Porter, D.A.; Easterling, E. E. *Phase Transformation in Metals and Alloys*, 2nd ed.; CRC Taylor and Francis: Boca Raton, FL, 2004; pp 112–117.
- (24) Gallea, F.; Li, Z.; Zhang, Z. *Appl. Phys. Lett.* **2006**, 89, 193111-1-3.